ROYAL SOCIETY
OF CHEMISTRY

PAPER

Check for updates

Tungsten dichalcogenide $WS_{2x}Se_{2-2x}$ films *via* single source precursor low-pressure CVD and their (thermo-)electric properties†

V. Sethi, [a] D. Runacres, [b] V. Greenacre, [b] Li Shao, [b] A. L. Hector, [b] W. Levason, [b] C. H. de Groot, [a] G. Reid *[b] and R. Huang *[a]

Semiconducting transition metal dichalcogenides have gained increased interest as potential alternatives to graphene due to their tunable electronic bandgaps. In this study, we present the deposition of stoichiometric $WS_{2x}Se_{2-2x}$ ($0 \leq x \leq 1$) binary and ternary thin films using the single source precursors, $[WECl_4(E'^nBu_2)]$ (E = S or Se; E' = S or Se), *via* low-pressure chemical vapour deposition. Compositional and structural characterisations of the deposits have been performed by grazing-incidence X-ray diffraction, scanning electron microscopy, X-ray photoelectron spectroscopy, and Raman spectroscopy, confirming the phase purity and stoichiometry. Electrical characterisation *via* Hall measurements reveals high electrical conductivities for those films. Such high conductivity is likely related to Se and S vacancies in the films and can be tuned through an annealing process. The thermoelectric capabilities of the $WS_{2x}Se_{2-2x}$ have been characterised with the use of variable-temperature Seebeck measurements, showing a peak power factor of 6 $\mu W\ m^{-1}\ K^{-2}$ for the as-deposited WS_2 film at 553 K.

1. Introduction

The discovery of graphene's extraordinary electrical properties has paved the way for faster and more efficient electronic devices. However, the absence of an electronic bandgap hinders potential applications.[1] The inorganic analogues of graphene, layered transition metal dichalcogenides (TMDCs), ME_2 (M = Nb, Ta, Mo, W, V, *etc.*; E = S, Se, or Te) do possess an electronic band gap with the magnitude and specific electronic properties dependent on the choice of metal and chalcogen. These unique semiconducting properties have attracted tremendous interest to explore TMDCs for the next generation of electrical and optical devices.[2]

Among the family of TMDCs, tungsten-based dichalcogenides (*e.g.* WS_2, WSe_2, $WS_{2x}Se_{2-2x}$) are of interest due to the natural abundance of W in the earth's crust, low-toxicity and cost-effectiveness.[3,4] These advantages have recently gained increased attention within the field of Li-ion batteries where WS_2 and WSe_2 have been identified as potential anode materials. However, integration has been hindered by intrinsically low electrical conductivities, making highly conductive WS_2 and WSe_2 of great interest.[5-7] The fabrication of atomically thin

monolayered films of these materials lends itself to integration into transistor-based devices, with the tuning of electrical performance allowing control of the on-off bias of these devices, as well as a reduction in quantum tunnelling effects.[8,9] The ability to tune the electronic performance of these materials also benefits a multitude of optoelectronic applications, including photodetectors and light-emitting diodes, which allows for the tailoring of devices for specific photoelectronic applications.[10,11]

Thin-film TDMCs can be grown *via* various approaches, including mechanical/liquid exfoliation,[12,13] sputtering,[14] pulsed layer deposition,[15] atomic layer deposition,[7] and molecular beam epitaxy.[16] The preparation of binary WE_2 (E = S, Se) thin films is usually achieved by sulfurization or selenization of WO_3 thin films, followed by an annealing process.[17,18] Chemical vapour deposition (CVD) is a low-cost and versatile deposition technique for semiconductor alloys. It is widely used in industry with most processes using dual or multiple precursor sources, each of which delivers one of the required elements. Several CVD approaches have been employed for the deposition of binary or ternary tungsten-based TMDCs, most of which use precursor sources such as WF_6 + H_2S; or WCl_6, $WOCl_4$ or $W(CO)_6$ with thiols.[19-32] In addition, aerosol-assisted CVD (AACVD) of WS_2 from the dithiocarbamate complex $[WS(S_2)(S_2CNEt_2)_2]$, and of $Mo_{1-x}W_xS_2$ from a mixture of $[WS(S_2)(S_2CNEt_2)_2]$ and $[Mo(S_2CNEt_2)_4]$ have been reported.[33,34]

Compared with dual/multiple source precursors, single source precursors (SSPs), which contain the metal and chalcogen(s) within a single molecule can potentially offer better

aSchool of Electronics and Computer Science, University of Southampton, Southampton, SO17 1BJ, UK. E-mail: r.huang@soton.ac.uk

bSchool of Chemistry, University of Southampton, Southampton, SO17 1BJ, UK. E-mail: G.Reid@soton.ac.uk

† Electronic supplementary information (ESI) available. See DOI: https://doi.org/10.1039/d3ta00466j

This journal is © The Royal Society of Chemistry 2023

J. Mater. Chem. A, 2023, 11, 9635–9645 | 9635

control of deposit stoichiometry, cost-effective use of reagents, easier-to-handle precursors and, in some cases, the ability to selectively deposit the chalcogenides onto nano-patterned substrates.[35] We recently reported the first single source low-pressure CVD reagent for WS_2, the dinuclear $[(WSCl_4)_2(^iPrSCH_2CH_2S^iPr)]$.[36] This success was very encouraging given the high molecular weight of the complex. Although the films produced were of good quality, we noted that a considerable residue remained after the vaporisation of the reagent, and deposition occurred only over a limited area of the substrate. We, therefore, sought to develop a new reagent that would maintain or improve the film quality, deposit more evenly and continuously over a larger substrate area, and which would vaporise completely under the experimental conditions. W(VI) complexes of monothioethers could be a potential option. However, the only known example, $[WSCl_4(SMe_2)]$,[36] is unsuitable since it lacks a low energy decomposition route, hence we considered complexes containing thioethers with longer alkyl chains, specifically containing β-hydrogen atoms. In previous work on other metal sulfide materials, including Nb,[22,37] Sn[38] and Mo,[39] we found that precursors incorporating thioethers with n-butyl substituents proved particularly suitable. The ^nBu group offers a β-hydride elimination route, and its complexes are often low melting or waxy solids, implying low lattice energies that aid vaporisation. S^nBu_2 is also cheap and commercially available. Recently, we have shown that $[WSeCl_4(Se^nBu_2)]$ is a suitable precursor for growth of WSe_2 thin films via CVD.[40]

We report here the development and application of new, tailored mononuclear complexes, $[WECl_4(E'^nBu_2)]$ (E = S, Se; E' = S, Se), designed as single source precursors for the low-pressure CVD (LPCVD) growth of tungsten dichalcogenides. By selecting the different combinations of E and E' in the precursor, we could not only deposit thin films of the binary WS_2 and WSe_2, but also, for the first time, the ternary $WS_{2x}Se_{2-2x}$ films. Moreover, electrical characterisation on the as-deposited $WS_{2x}Se_{2-2x}$ ($0 \leq x \leq 1$) thin films reveal high electrical conductivities with an increase of several orders in carrier concentration when compared to literature.[41–43] This high conductivity is likely related to the substantial number of Se and S vacancies within the films. Such high conductivity can be tuned via an annealing process to reduce the vacancy concentration. The capability of controlling the electrical conductivity of $WS_{2x}Se_{2-2x}$ films via the choice of single source precursor and the annealing process can be beneficial for its application in advanced optical switches as well as transistor device mobility engineering.[44–46]

2. Material preparation and methods

2.1 Single source precursor synthesis

S^nBu_2 was purchased from Sigma-Aldrich and used as received. $WSCl_4$,[36] $WSeCl_4$,[40] and Se^nBu_2[47] were prepared as previously described. All reactions were conducted under a dry dinitrogen atmosphere using Schlenk, vacuum line, and glovebox techniques. CH_2Cl_2 was dried by distillation from CaH_2 and n-hexane from Na and stored over activated 4 Å molecular sieves.

Dry NMR solvents were also stored over 4 Å sieves. IR spectra were recorded as Nujol mulls between CsI plates using a Perkin-Elmer Spectrum 100 spectrometer over the range of 4000–200 cm^{-1}. Raman spectra used a Renishaw InVia Raman Microscope with a 100 mW He–Ne 785 nm laser. NMR spectra were recorded using a Bruker AVII 400 spectrometer. ^1H NMR spectra were referenced to residual solvent resonances and $^{77}Se\{^1H\}$ NMR spectra to external neat $SeMe_2$.

2.1.1 Precursor synthesis

2.1.1.1 [WSCl_4(S^nBu_2)] (1). A solution of di-n-butyl sulfide (0.041 g, 0.28 mmol) in dichloromethane (5 mL) was added slowly to a suspension of $WSCl_4$ (0.100 g, 0.28 mmol) in dichloromethane (5 mL). The dark red solution was stirred for 1 h and then reduced to dryness in vacuo, leaving a viscous red oil. IR spectrum (Nujol, ν/cm^{-1}): 538 s (W=S), 348 br s (W–Cl) (Fig. S1†). Raman spectrum (ν/cm^{-1}): 535 s (W=S), 379 (W–Cl) (Fig. S2†). ^1H NMR (CDCl$_3$): 2.74 (br, [2H], CH$_2$), 1.83 (br, [2H], CH$_2$), 1.52 (br, [2H], CH$_2$), 0.96 (t, [3H], CH$_3$) (Fig. S3†).

2.1.1.2 [WSCl_4(Se^nBu_2)] (2). A solution of di-n-butyl selenide (0.135 g, 0.69 mmol) in dichloromethane (5 mL) was added slowly to a suspension of $WSCl_4$ (0.250 g, 0.69 mmol) in dichloromethane (5 mL). The dark red solution was then stirred for 1 h, before the volatiles were removed in vacuo, leaving a dark red viscous oil. IR spectrum (Nujol, ν/cm^{-1}): 533 s (W=S), 375 s (W–Cl) (Fig. S4†). Raman spectrum (ν/cm^{-1}): 536 s (W=S), 322 br (W–Cl) (Fig. S5†). ^1H NMR (CD$_2$Cl$_2$): δ = 2.74 (br, [2H], CH$_2$), 1.74 (br, [2H], CH$_2$), 1.46 (br m, [2H], CH$_2$), 0.94 (t, [3H], CH$_3$). $^{77}Se\{^1H\}$ NMR (CD$_2$Cl$_2$): δ = +298.6 (s, $^1J_{WSe}$ = 79 Hz) (Fig. S6–S8†).

2.1.1.3 [WSeCl_4(S^nBu_2)] (3). A solution of di-n-butyl sulfide (0.043 mL, 0.25 mmol) in dichloromethane (5 mL) was slowly added to a suspension of $WSeCl_4$ (0.100 g, 0.25 mmol) in dichloromethane (5 mL) to form a green solution. After stirring for 10 min, the solution was concentrated in vacuo to a deep green oil. IR spectrum (Nujol, ν/cm^{-1}): 368 s (W=Se), 343 s (W–Cl) (Fig. S9†). Raman spectrum (ν/cm^{-1}): 379 s (W=Se), 344 s (W–Cl) (Fig. S10†). ^1H NMR (CD$_2$Cl$_2$): δ = 2.58 (br, [2H], CH$_2$), 1.69 (br, [2H], CH$_2$), 1.48 (br m, [2H], CH$_2$), 0.93 (t, [3H], CH$_3$) (Fig. S11†).

2.1.1.4 [WSeCl_4(Se^nBu_2)] (4). $[WSeCl_4(Se^nBu_2)]$ (4) was prepared by the literature method.[40]

Fresh samples of single source precursors (SSPs) (1–4) were prepared just prior to the CVD experiments, as (3) and (4) in particular, tend to decompose over a period of a few hours.
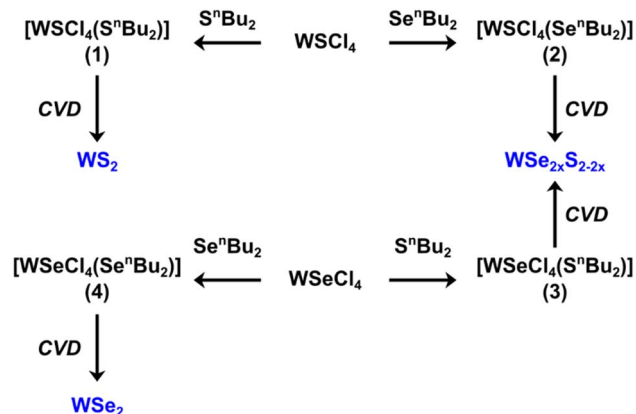
A molecular representation of the SSPs (1–4) is shown in Scheme 1.

2.2 Low-pressure CVD onto fused quartz substrates

The binary and ternary TMDC films were deposited via low-pressure CVD using precursors (1–4) as shown in Scheme 1, with a schematic diagram of the CVD process provided in Fig. 1. The temperature gradient through the length of the furnace was measured using a thermocouple.

In an N_2 purged glove box the precursor (20–30 mg) was loaded into the precursor bulb at the closed end of a silica tube, silica substrates (ca. $1 \times 8 \times 20$ mm^3) were then positioned end-

9636 | *J. Mater. Chem. A*, 2023, **11**, 9635–9645

This journal is © The Royal Society of Chemistry 2023

Scheme 1 The methods used for the synthesis of precursors (**1–4**) and the thin film TMDC material (blue) obtained from low-pressure CVD from each.
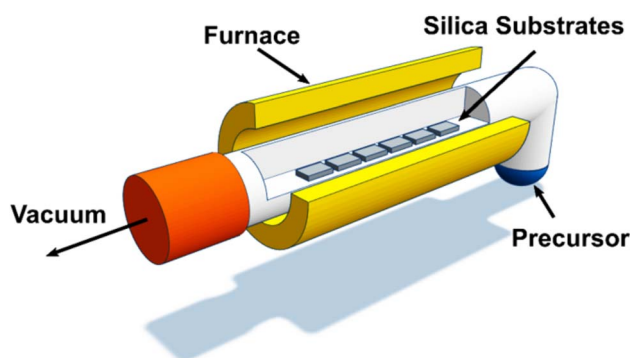

Fig. 1 A visual representation of our low-pressure chemical vapour deposition (LPCVD) setup, consisting of an open-ended quartz tube held under vacuum to draw the volatilised precursor through the heated zone and across the silica substrates.

to-end lengthways along the tube outwards from the precursor. The tube was then set horizontally in a furnace so that the substrates were in the heated zone and the precursor protruded *ca.* 1 cm ((**1**) and (**2**)) or *ca.* 4 cm ((**3**) and (**4**)) out of the furnace. The tube was evacuated to 0.1 mmHg and the furnace was heated to 700 °C and held for 10–15 minutes to allow the temperature to stabilise. The tube was gradually moved towards the hot zone until evaporation of the precursor was observed. The position was maintained for *ca.* 15–20 min, or until no further evaporation occurred; negligible residue was observed in the precursor bulb. The tube was then cooled to room temperature and the substrates were removed for characterisation. Brown films were obtained from precursor (**1**) (actual deposition temperature range = 624–650 °C), (**2**) (actual deposition temperature range = 593–652 °C) and (**3**) (actual deposition temperature range = 563–593 °C), while silver films were obtained from precursor (**4**) (actual deposition temperature range = 624–650 °C) as described.[40] Good film coverage over the substrate was observed for all four films with no variation of morphology over the substrate. The four films are hereafter referred to as films A, B, C and D, respectively.

2.3 $WS_{2x}Se_{2-2x}$ film characterisation ($0 \leq x \leq 1$)

The $WS_{2x}Se_{2-2x}$ thin films (A, B, C and D) deposited from (**1–4**) were characterised using a combination of techniques. The morphology was investigated by scanning electron microscopy (SEM) using a Jeol JSM 7500F FESEM with an accelerating voltage of 5 kV. X-ray diffraction (XRD) patterns were collected in grazing incidence mode ($\theta_1 = 1°$) using a Rigaku SmartLab diffractometer (Cu-K$_\alpha$, $\lambda = 1.5418$ Å) with parallel X-ray beam and a Hypix detector operated in 1D mode. Phase matching and lattice parameter calculations were undertaken using the PDXL2 software package[48] and diffraction patterns from ICSD.[49,50] X-ray photoelectron spectroscopy (XPS) data were obtained using a Thermo Scientific Theta Probe system with Al-K$_\alpha$ radiation (photon energy = 1486.6 eV). All peaks are calibrated against the adventitious C 1s peak at 284.6 eV.[51] All films were subject to an *in situ* 30 s Ar etch to remove surface oxygen prior to the measurement. Raman spectra of the deposited films were measured at room temperature on a Renishaw InVia Micro Raman Spectrometer using 532 nm excitation. The incident laser power was 0.1 mW for all samples with a 50× magnification, which resulted in a spot size of 1 μm diameter.

Electrical characterisation was conducted using the van der Pauw configuration using a Nanometrics HL5500 Hall effects system across a temperature range of 150 to 450 K using liquid N$_2$. Electrical conductivity (σ) measurements were also conducted *in situ* with Hall measurements to determine carrier mobility (μ) and carrier density (n) at a magnetic field of 0.5 T. A visual depiction of a typical Hall measurement is displayed in Fig. S12.† The contacts from the probes to the samples were checked carefully before each measurement. *I–V* curves were recorded before each measurement to ensure ohmic conduction as well as to optimise the current for a maximised voltage signal (20 mV). Variable-temperature Seebeck coefficients and electrical resistivity were measured using a JouleYacht thin-film thermoelectric parameter test system (MRS-3L). The system was calibrated using a nickel foil reference standard, and the measurement accuracy was found to be within 5%. Seebeck coefficients were determined using the differential method with a maximum temperature difference of 10 K. This system allows further extension of the electrical conductivity measurement range to *ca.* 550 K, as well as simultaneous measurements of thermopower.

3. Results and discussion

3.1 Composition, morphological, and structure properties

Top-view SEM images were taken to reveal the morphological properties of the four as-deposited $WS_{2x}Se_{2-2x}$ films, which are shown in Fig. 2. From inspection, all four precursors yield films with continuous polycrystalline layers and slightly varying grain morphologies depending on the choice of SSP. All films have formed structures with a preferred orientation parallel to the substrate surface, reflecting the layered nature of TDMCs.[52] The continuity of the films is further supported by the cross-sectional SEM images shown in Fig. S13.† EDX mappings were also conducted on all four films and are presented in
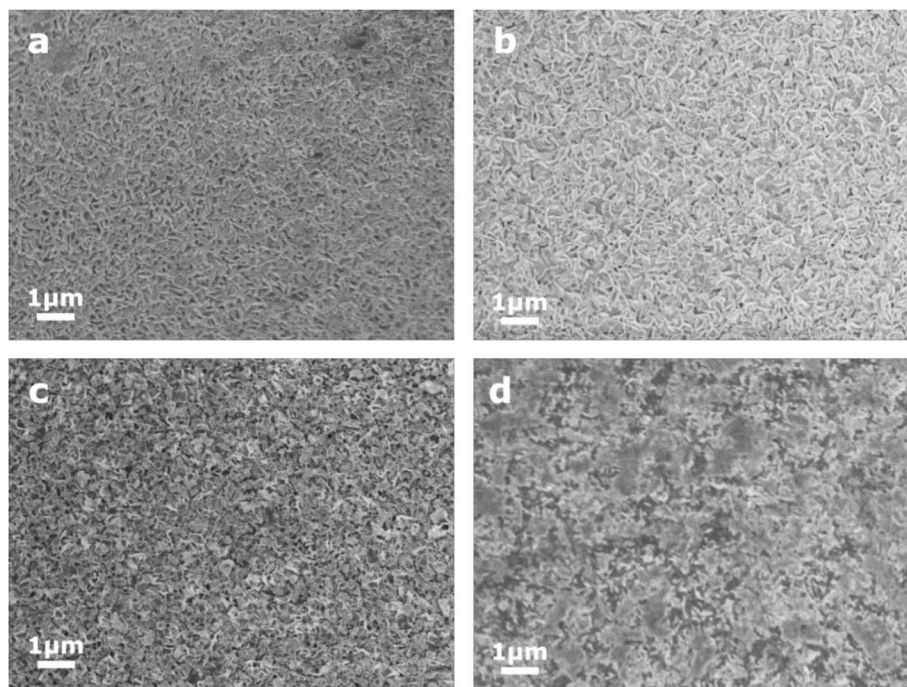
This journal is © The Royal Society of Chemistry 2023

J. Mater. Chem. A, 2023, **11**, 9635–9645 | **9637**

Fig. 2 Top-view SEM images of $WS_{2x}Se_{2-2x}$ films produced *via* low-pressure CVD using SSPs (**1**) to (**4**), respectively.

Fig. S14.† It is clear that all elements are uniformly distributed, further confirming the quality of the film deposited by our SSPs.

The phase purity and crystallinity of the as-deposited films were examined by grazing incidence XRD analysis and are shown in Fig. 3. All films are isostructural, with no other phases detectable. The XRD patterns are consistent with the 2H coordination in space group $P6_3/mmc$ which has two layers per unit cell. All films were dominated by the 002 reflections, suggesting a preferred orientation in the $\langle 00l \rangle$ direction. A systematic shift

of the characteristic diffraction peaks with increasing Se content is also evident as the WS_2 lattice expands with the incorporation of Se into the film. For the ternary films (B and C) this peak is located between those for the binary materials, 14.3° (A: WS_2) and 13.6° (D: WSe_2).

The XRD indicated our as deposited films adopt the 2H structure, but Raman can be more sensitive to structure in small crystallite materials. The 2H structure is expected to result in 18 potential phonon modes with 3 of them Raman active with A_{1g},
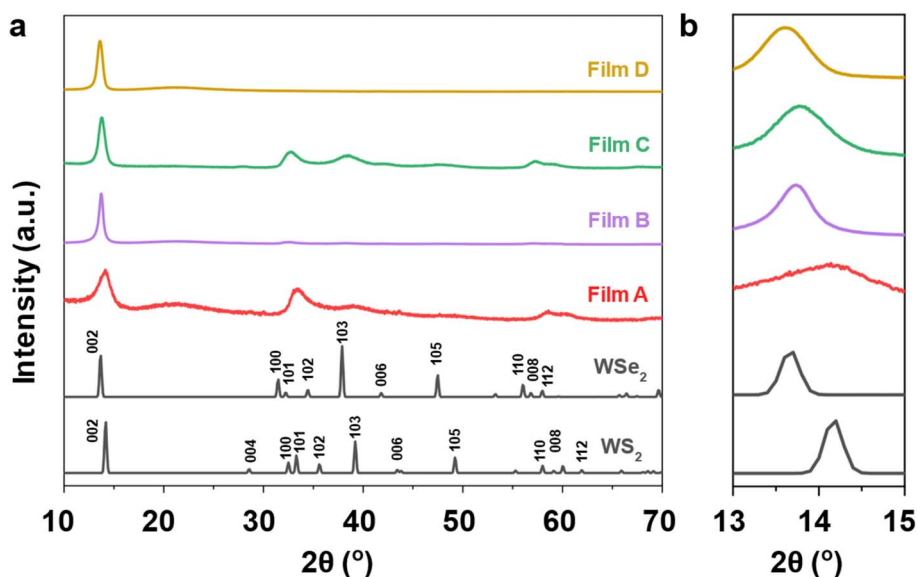

Fig. 3 (a) Grazing incidence X-ray diffraction patterns of the as-deposited $WS_{2x}Se_{2-2x}$ films from (**1–4**), together with reference XRD patterns for both WS_2 and WSe_2 (black);[49,50] (b) an expansion of the range 13° and 15° to illustrate the shift of the 002 peaks.
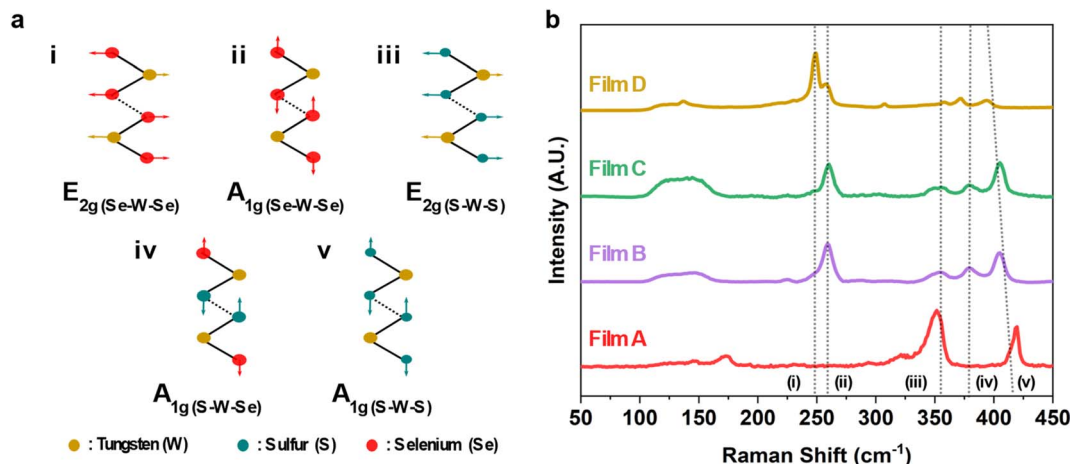
Fig. 4 (a) A visual depiction of E_{2g} and A_{1g} vibrational modes for all possible binding configurations found within the binary and ternary films. (b) Raman spectral scan presented over a range of 50–450 cm^{-1}, of the as-deposited $WS_{2x}Se_{2-2x}$ films.

E_{1g} and E_{2g} symmetry.[53] The A_{1g} represents the out-of-plane symmetrical stretching and the E_{1g} and E_{2g} modes signify the doubly degenerate asymmetric and symmetric in-plane vibrations within TMDCs, as visually depicted in Fig. 4a.[53] However, in the Raman backscattering configuration used in this study, only the A_{1g} and E_{2g} modes can be observed due to the asymmetric stretching and the double degeneracy of the E_{1g} modes.[53] The presence of these two Raman active modes is evident in all of the as-deposited films, as seen in Fig. 4b. The characteristic peaks, namely, (i) $E_{2g(Se-W-Se)}$ and (ii) $A_{1g(Se-W-Se)}$ are located at 248.7 cm^{-1} and 258.5 cm^{-1} respectively. These are related to the WSe_2 film (D from precursor (**4**)).[54] The Raman spectra of the as-deposited WS_2 film (A from precursor (**1**)) align well with reports from literature with peaks (iii) $E_{2g(S-W-S)}$ and (v) $A_{1g(S-W-S)}$ at 353.8 cm^{-1} and 418.5 cm^{-1} respectively, with a peak separation of 68.4 cm^{-1}.[53,55] It should be noted that the peak at *ca.* 350.1 cm^{-1} is a convolution of two modes: the aforementioned $E_{2g(S-W-S)}$ mode and the 2LA(M) mode. The latter of these is a second-order longitudinal acoustic phonon. This feature is often prevalent in monolayer and few-layer WS_2.[56]

Interestingly, the two ternaries (B and C from precursors (**2**) and (**3**)) also give rise to an additional peak located at *ca.* 380 cm^{-1}. This is believed to be related to the out-of-plane vibration of both S and Se coordinated to a central W atom and will be hereon referred to as the (iv) $A_{1g(S-W-Se)}$ mode.[54] The presence of this peak, along with the significant suppression of the peaks associated with WS_2 and WSe_2, signify the successful deposition of ternary $WS_{2x}Se_{2-2x}$. The broad feature located at *ca.* 150 cm^{-1} is reported to be a superposition of two second-order modes, namely the $E_{2g(S-W-S)}$–$LA_{(S-W-S)}$ and the $A_{1g(Se-W-Se)}$–$LA_{(Se-W-Se)}$.[54] The significant enhancement of this peak in the ternary films further supports the presence of both S and Se within the film. A redshift was observed in the (v) $A_{1g(S-W-S)}$ mode with increased Se content within the film. This behaviour has been previously reported in $WS_{2x}Se_{2-2x}$ alloys.[54]

The composition of the as-deposited TMDC films was investigated *via* X-ray photoelectron spectroscopy (XPS). Presented in Fig. S15† are the survey scans for all four as-deposited films. The films are free of impurities (*e.g.* C, Cl) which speaks to their high quality. From the survey scan, the spectrum shows
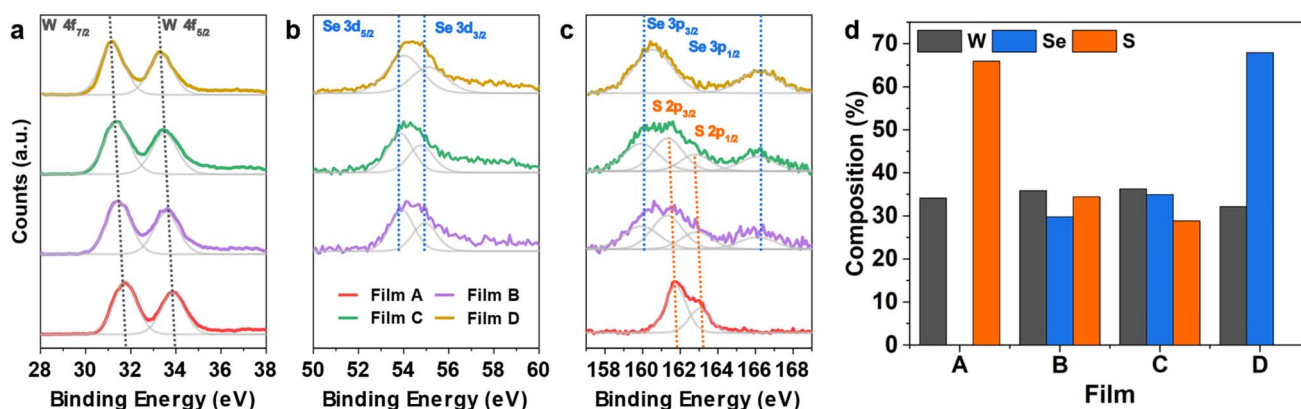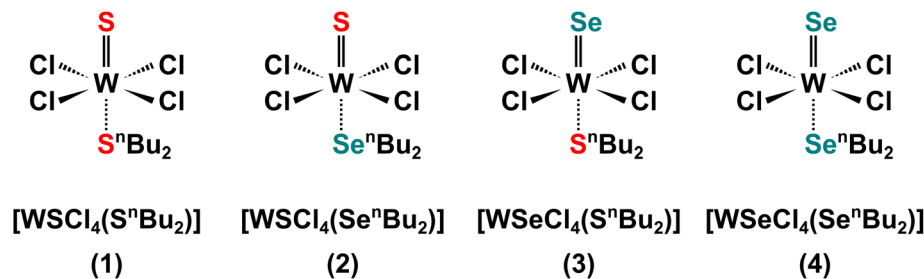

Fig. 5 Elemental XPS scans of (a) W 4f, (b) Se 3d and (c) S 2p for all as-deposited $WS_{2x}Se_{2-2x}$ films deposited from precursors (**1–4**). (d) Composition of all the as-deposited films deposited from precursors (**1–4**).

This journal is © The Royal Society of Chemistry 2023

J. Mater. Chem. A, 2023, **11**, 9635–9645 | **9639**

$[WSCl_4(S^nBu_2)]$ **(1)** $[WSCl_4(Se^nBu_2)]$ **(2)** $[WSeCl_4(S^nBu_2)]$ **(3)** $[WSeCl_4(Se^nBu_2)]$ **(4)**

Scheme 2 A molecular representation of precursors (**1–4**).

peaks consistent with both binary and ternary WS_2 and WSe_2 films with the related orbitals labelled.[14,57] Fig. 5a–c presents the elemental scans of the W 4f, S 2p and Se 3d orbitals for the four films. It is worth noting that due to the overlap of atomic orbitals of the Se 3p and S 2p sub-shells, deconvolution of the S and Se contributions is required for the alloyed films.

In the W 4f scan (Fig. 5a) a single doublet formation is observed in all four films, which arises from spin–orbit coupling (W $4f_{7/2}$ and W $4f_{5/2}$). The position of the doublet indicates the W^{4+} oxidation state corresponding to the presence of tungsten chalcogenide bonds within the film.[57,58] The absence of a W^{6+} oxidation state is characteristic of W-based TDMCs.[57,59] The substitution of sulfur with selenium causes a small shift in the peaks related to W 4f and the S 2p orbitals to lower binding energies. This is indicated by the grey projection lines shown in Fig. 5a and agrees with previously reported values for the WS_2 and WSe_2 systems.[60]

Similarly, from the elemental scan of the Se 3d orbital (see Fig. 5b), two significant peaks were observed for films B to D, notably the Se $3d_{5/2}$ and Se $3d_{3/2}$ positioned at *ca.* 54 eV and *ca.* 54.8 eV respectively. These peaks are related to the Se^{2-} oxidation state indicating Se bonded to W.[61] The elemental scan of S
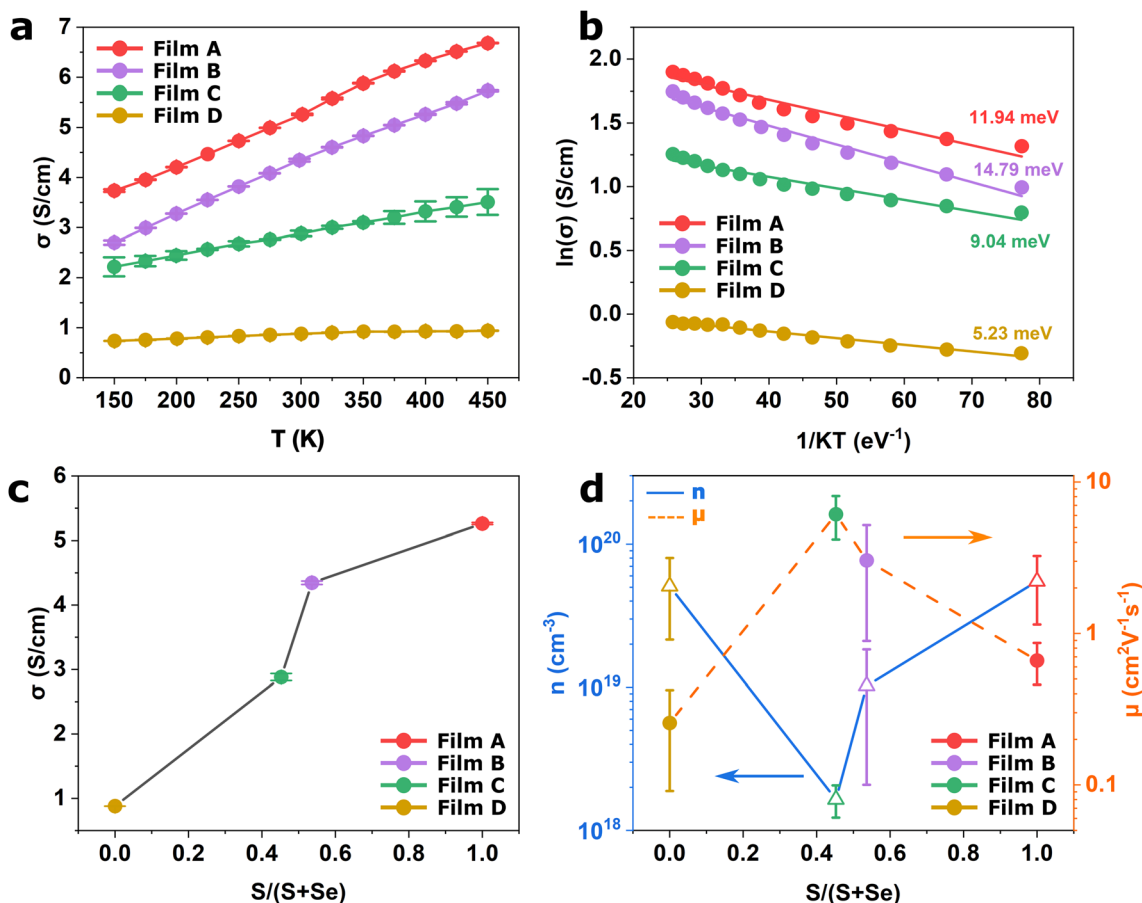

Fig. 6 (a) Temperature-dependent electrical conductivity, (b) Arrhenius plot for $WS_{2x}Se_{2-2x}$ films deposited from precursors (**1–4**). (c) Electrical conductivity and (d) Hall measurements against the chalcogenide content of the films.

9640 | *J. Mater. Chem. A*, 2023, **11**, 9635–9645

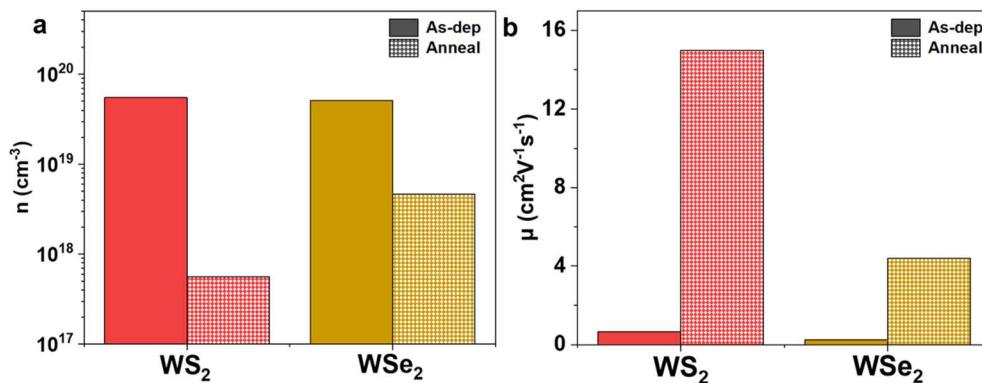This journal is © The Royal Society of Chemistry 2023

Fig. 7 (a) Carrier concentration and (b) carrier mobility of the as-deposited binary films, WS_2 (red) and WSe_2 (orange). Compared with the films annealed at 500 °C in the respective chalcogenide atmospheres.

2p peaks on film A presents a doublet located at 161.5 eV and 162.7 eV, respectively, which correspond to $2p_{3/2}$ and $2p_{1/2}$ states in WS_2,[62] as shown in Fig. 5c. In terms of films B and C, XPS scans reveal the presence of both S and Se in the film through the existence of two doublets in the range 158 to 170 eV (Fig. 5c). This suggests that both precursors have successfully produced ternary tungsten chalcogenide films.

For accurate determination of composition, the peak separations were fixed for both the S and the Se doublets, with peak separations of 1.2 and 6.1 eV respectively, agreeing well with the literature.[62] The doublet related to S 2p orbital is located at 161.2 and 162.4 eV, corresponding to the spin up (S $2p_{3/2}$) and spin down (S $2p_{1/2}$) states.[62] The remaining area is associated with the Se 3p orbital which is situated at 160 and 166.1 eV, relating to the spin-up (Se $3p_{3/2}$) and spin-down (Se $3p_{1/2}$) states. The derived compositions of the two ternary films are shown in Fig. 5d, together with the two binaries. With films from (**1**) and (**4**) being stoichiometric WS_2 and WSe_2, respectively, precursors (**2**) and (**3**) each produced ternary films with 33% of W in both films. The stable W content suggests the successful deposition of ternary $WS_{2x}Se_{2-2x}$ and also indicates both S and Se bound to a central W atom.[62] Interestingly, precursor (**3**) produces

a ternary film with a slightly lower sulfur concentration ($x = 0.40$) than that of the film from (**2**) ($x = 0.48$). We believe the slight difference in the composition originates from the different W–S/Se bonding present in precursors (**2**) and (**3**). While former has a W=S double bond and a weaker W ← Se coordinate bond involving the neutral selenoether (Se^{n}Bu$_2$), on the other hand the latter features a W=Se double bond and a W ← S coordinate bond (shown in Scheme 2). We believe that the chalcogenide bound to the W with a double bond in the precursor is more strongly bound and hence is dominant in the final film composition, which leads to the slightly higher S composition in film B and higher Se composition in film C. It is worth mentioning that it is possible to further control the composition by combination of the various single source precursors developed in this work with different ratios. This is enabled by the analogous nature of our 4 precursors and their compatible deposition temperatures.

3.2 Electrical characterisation

The electrical properties of the $WS_{2x}Se_{2-2x}$ films deposited in this work were investigated. Fig. 6a presents the temperature-dependent electrical conductivity of the four films. Very
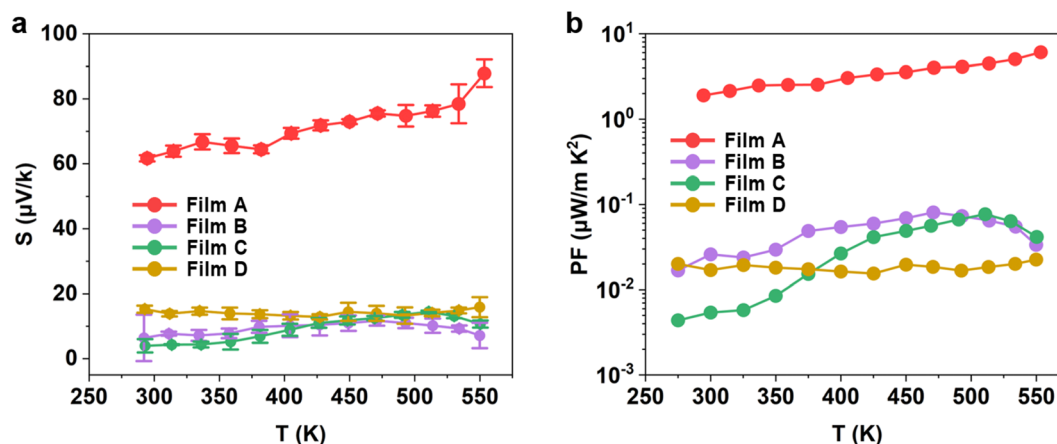

Fig. 8 Temperature-dependent (a) Seebeck, and (b) power factor measurements for the $WS_{2x}Se_{2-2x}$ films deposited from precursors (**1–4**).

interestingly, all films have relatively high electrical conductivities over 0.8 S cm^{-1} across the temperature range of 150 to 450 K. It is known that TMDCs can adopt two crystal structures, a metallic 1T phase and a semiconducting 2H phase, with the 1T phase being more favoured due to the larger electrical conductivity. However, issues regarding 1T phase stability have restricted the progress of this phase as it commonly reverts to the more stable 2H phase.[63] In this work, despite the films all being found to be in the 2H coordination (illustrated by the XRD and the Raman spectra), all films yielded a strikingly high electrical conductivity when compared to literature.[41,64–66]

The 2H coordination would also suggest that the films will display semiconducting behaviour which is intrinsically temperature dependent due to the promotion of charge carriers to the conduction band upon absorption of thermal energy. For thermally activated conduction in semiconducting materials, the electrical conductivity (σ) can be expressed by the relation shown in eqn (1).[67]

$$\sigma = \sigma_0 \exp\left(\frac{-E_a}{k_B T}\right) \tag{1}$$

where σ_0 is a constant, k_B is Boltzmann's constant and E_a is the thermal activation energy which defines the energy difference between the Fermi level (E_F) and the conduction band (E_C). Fig. 6b displays the Arrhenius plots of all four films, from which the derived activation energies are of low magnitude in the range of 5 to 15 meV. Such weak temperature dependence of the electrical conductivity suggests a semi-metallic behaviour, in contrast to what is often exhibited by TDMCs.[3] The electrical conductivity appears to correlate with the sulfur content of the film, as displayed in Fig. 6c. The WSe$_2$ (D from precursor (4)) has the lowest electrical conductivity among the four films at 300 K. The conductivity increases with an increasing amount of sulfur in the ternary films, reaching the highest value of 5.2 S cm^{-1} for the binary WS$_2$.

To shed more light on this behaviour, room temperature Hall measurements were conducted to explore the mechanism that governs the high electrical conductivity. Displayed in Fig. 6d is the majority carrier concentration (blue) and the carrier mobility (orange) as a function of the sulfur content in the film. It can be observed that all four films feature high carrier concentrations in the order of 10^{18} to 10^{20} cm^{-3}. These are significantly larger than those typically reported for TMDCs[41,43] and contribute to the high conductivities measured for the films. Such high carrier concentration is likely due to the formation of vacancies at the chalcogenide site on the crystallite surface. These vacancies act as self-dopants that enhance the carrier concentration of the film.[68] On the other hand, the vacancies also act as scattering centres, which hinder carrier mobility,[69] resulting in lower mobility compared with reports in literature.[70,71] It is also likely that the platelet-like structures encompassed within the films also hinder carrier mobility through grain boundary scattering.[72] It is worth mentioning that all four films demonstrate p-type conductivity. This is unsurprising for the WSe$_2$ films which generally favours p-type conduction and have been integrated into p-type field effect transistors.[73,74] However, WS$_2$ films have been reported to display ambipolar behaviour in which concentrations of electrons and holes are of similar magnitudes.[75] The absence of an anion (i.e. S vacancy), has been suggested to act as electron trap, with electrons aggregating around the anionic site.[68,75] This would suppress the n-type conduction channel leading to the p-type behaviour being exhibited by the film. Interestingly, the two binaries show higher carrier concentrations than the ternaries. This implies that the binary films have a higher tendency to form surface vacancies compared to their alloyed counterparts.

To verify whether the vacancies drive the semi-metallic behaviour displayed in the as-deposited films, the two binary WS$_2$ and WSe$_2$ films were annealed in sulfur and selenium atmospheres, respectively, at 500 °C for 2 hours with the aim to suppress the vacancies formed at the chalcogenide site. Fig. 7 presents the effects on (a) carrier concentration and (b) carrier mobility for the as-deposited and post-annealed binary films. The annealed WS$_2$ film was observed to have a near two orders of magnitude drop in carrier concentration from 5.50 × 10^{19} cm^{-3} to 5.62 × 10^{17} cm^{-3}, along with an enhancement of carrier mobility (from 0.66 cm^2 V^{-1} s^{-1} to 14.99 cm^2 V^{-1} s^{-1}). Similarly, annealing the WSe$_2$ film in a selenium atmosphere also resulted in a significant drop in carrier concentration from 5.08 × 10^{19} cm^{-3} to 4.68 × 10^{18} cm^{-3} with a concurrent increase of carrier mobility from 0.26 cm^2 V^{-1} s^{-1} to 4.39 cm^2 V^{-1} s^{-1}. Both cases strongly suggest that the suppression of chalcogen (i.e. sulfur and selenium) vacancies within the film upon annealing can induce significant changes in the self-doping level of our tungsten TMDCs. This offers an avenue for tuning the electrical performance of the TMDC films with an annealing process which can be beneficial for enhancing the performance of field effect transistors (FETs), photodiodes and optoelectronic devices.[57,76,77]

The phenomenon of thermoelectric power generation is based on the Seebeck effect, which can be understood by the relation shown in eqn (2).[78]

$$S = -\frac{V}{\Delta T} \tag{2}$$

where V is the Seebeck potential and ΔT is the applied temperature difference. This phenomenon allows for the direct conversion of thermal energy to electrical energy. The potential arises due to the net diffusion of electrons (n-type) and holes (p-type), from the hot side to the cold side, due to the charge carriers on the hot side having greater kinetic energy. The thermoelectric performance of the four WS$_{2x}$Se$_{2-2x}$ films produced in this work was evaluated via temperature-dependent Seebeck measurements as shown in Fig. 8. Positive Seebeck coefficient (S) values were obtained for all films, indicating p-type conduction, consistent with the Hall measurement results (Fig. 8a). Among the four films, binary WS$_2$ demonstrates a Seebeck coefficient of ca. 61 μV K^{-1} at 300 K. This is significantly higher than those of the other three films which range from 3 μV K^{-1} to 15 μV K^{-1}. This enhancement is potentially due to the grains formed for the WS$_2$ film being considerably smaller, as indicated by the broadening of the 002 peak displayed in Fig. 4.[79] Smaller grains lead to energy filtering

9642 | J. Mater. Chem. A, 2023, **11**, 9635–9645

This journal is © The Royal Society of Chemistry 2023

effects realised by enhanced grain boundary scattering, which suppresses the mean free path of the material's charge carriers, thus enhancing S.[80] The Seebeck coefficient increased to a peak of 88 μV K^{-1} at 553 K.

A useful parameter that is used to quantify and optimise the electrical-dependent properties of a thermoelectric material is the power factor, with the relation shown in eqn (3).

$$PF = \sigma S^2 \qquad (3)$$

The improved Seebeck coefficient and the intrinsically high electrical conductivity of film A led to a peak power factor of 6 μW m^{-1} K^{-2} being achieved for the as-deposited WS$_2$ film at 553 K, as shown in Fig. 8b. The performance of the as-deposited WS$_{2x}$Se$_{2-2x}$ films created by such a simple and low-cost method is very encouraging. The enhanced electrical performance, as well as the ability to tune the performance, offer potential advantages regarding integration for a range of electrical and optical devices, as well as the potential fabrication of superlattice structures with alternating use of SSPs (1–4).[29,81]

4. Conclusions

In conclusion, this work reports the successful synthesis of a family of four distinct, but chemically quite analogous single source precursors, [WECl$_4$(E^{n}Bu$_2$)] (E = S, Se) suitable for the chemical vapour deposition of either binary or ternary WS$_{2x}$-Se$_{2-2x}$ thin films with good substrate coverage, high crystallinity and excellent stoichiometry, as confirmed by XRD, XPS and Raman measurements, along with significant evidence of the formation of W bound to both chalcogenides present in the alloyed films (S and Se). Hall measurements reveal that all the WS$_{2x}$Se$_{2-2x}$ films displayed p-type semi-metallic behaviour. The films yielded electrical conductivities ranging from 0.85 S cm^{-1} to 5 S cm^{-1} with the conductivity increasing with the S content of the film. This high conductivity can be ascribed to its high carrier concentration which is likely to originate from the formation of vacancies at the chalcogenide site. However, significant suppression of carrier mobility was noted, likely due to increased defect scattering. The level of vacancies can be modulated through an annealing process, which enables the potential for tuning the electrical performance *via* the deposition conditions.

Thermoelectric characterisation revealed a power factor of 6 μW m^{-1} K^{-2} for the as-deposited WS$_2$, which was driven by the significantly enhanced electrical conductivity and a thermopower of 88 μV K^{-1} at 553 K. The enhanced electrical performance of undoped WS$_{2x}$Se$_{2-2x}$ films, along with the deposition of pristine p-type WS$_2$ offers promising avenues for the thermoelectric development of these materials, with the potential for further enhancements being realised through greater control of crystal growth, *via* precise control of the deposition conditions. The capability of controlling the electrical properties of the WS$_{2x}$Se$_{2-2x}$ thin film through the selection of single source precursor and a simple annealing process certainly points towards the use of CVD-grown TMDC films in a wide range of electronic, thermoelectric and optical (nano)devices.

Author contributions

The manuscript was written through contributions of all authors. All authors have given approval to the final version of the manuscript.

Conflicts of interest

There are no conflicts to declare.

Acknowledgements

References

1 A. Chaves, J. G. Azadani, H. Alsalman, D. R. da Costa, R. Frisenda, A. J. Chaves, S. H. Song, Y. D. Kim, D. He, J. Zhou, A. Castellanos-Gomez, F. M. Peeters, Z. Liu, C. L. Hinkle, S. H. Oh, P. D. Ye, S. J. Koester, Y. H. Lee, P. Avouris, X. Wang and T. Low, *npj 2D Mater. Appl.*, 2020, **4**, 29.

2 J. Fan and M. Sun, *Chem. Rec.*, 2022, **22**, 1–34.

3 A. Eftekhari, *J. Mater. Chem. A*, 2017, **5**, 18299–18325.

4 Z. Zhang, P. Chen, X. Yang, Y. Liu, H. Ma, J. Li, B. Zhao, J. Luo, X. Duan and X. Duan, *Natl. Sci. Rev.*, 2020, **7**, 737–744.

5 J. Huang, X. Wang, J. Li, L. Cao, Z. Xu and H. Wei, *J. Alloys Compd.*, 2016, **673**, 60–66.

6 P. Zhou, G. Collins, Z. Hens, K. M. Ryan, H. Geaney and S. Singh, *Nanoscale*, 2020, **12**, 22307–22316.

7 D. K. Nandi, U. K. Sen, A. Dhara, S. Mitra and S. K. Sarkar, *RSC Adv.*, 2016, **6**, 38024–38032.

8 B. Zheng, D. Li, C. Zhu, J. Lan, X. Sun, W. Zheng, H. Liu, X. Zhang, X. Zhu, Y. Feng, T. Xu, L. Sun, G. Xu, X. Wang, C. Ma and A. Pan, *InfoMat*, 2020, **2**, 752–760.

9 H. S. Ra, M. H. Jeong, T. Yoon, S. Kim, Y. J. Song and J. S. Lee, *Adv. Sci.*, 2020, **7**, 2001475.

10 J. S. Ross, P. Klement, A. M. Jones, N. J. Ghimire, J. Yan, D. G. Mandrus, T. Taniguchi, K. Watanabe, K. Kitamura, W. Yao, D. H. Cobden and X. Xu, *Nat. Nanotechnol.*, 2014, **9**, 268–272.

11 J. Pu, H. Ou, T. Yamada, N. Wada, H. Naito, H. Ogura, T. Endo, Z. Liu, T. Irisawa, K. Yanagi, Y. Nakanishi, Y. Gao, M. Maruyama, S. Okada, K. Shinokita, K. Matsuda, Y. Miyata and T. Takenobu, *Adv. Mater.*, 2022, **34**, 2203250.

12 D. Xu, P. Xu, Y. Zhu, W. Peng, Y. Li, G. Zhang, F. Zhang, T. E. Mallouk and X. Fan, *ACS Appl. Mater. Interfaces*, 2018, **10**, 2810–2818.

13 B. Adilbekova, Y. Lin, E. Yengel, H. Faber, G. Harrison, Y. Firdaus, A. El-Labban, D. H. Anjum, V. Tung and T. D. Anthopoulos, *J. Mater. Chem. C*, 2020, **8**, 5259–5264.

This journal is © The Royal Society of Chemistry 2023

J. Mater. Chem. A, 2023, **11**, 9635–9645 | **9643**

14 Y. Koçak, Y. Akaltun and E. Gür, *J. Phys.: Conf. Ser.*, 2016, **707**, 012028.

15 F. Godel, V. Zatko, C. Carrétéro, A. Sander, M. Galbiati, A. Vecchiola, P. Brus, O. Bezencenet, B. Servet, M. B. Martin, B. Dlubak and P. Seneor, *ACS Appl. Nano Mater.*, 2020, **3**, 7908–7916.

16 B. Pielić, D. Novko, I. Š. Rakić, J. Cai, M. Petrović, R. Ohmann, N. Vujičić, M. Basletić, C. Busse and M. Kralj, *ACS Appl. Mater. Interfaces*, 2021, **13**, 50552–50563.

17 A. Thangaraja, S. M. Shinde, G. Kalita and M. Tanemura, *Mater. Lett.*, 2015, **156**, 156–160.

18 X. Di, F. Wang, J. Wei, B. Zhang, X. Lin and K. Zhang, in *China Semiconductor Technology International Conference 2019, CSTIC 2019*, Institute of Electrical and Electronics Engineers Inc., 2019, pp. 1–3.

19 J. R. Brent, N. Savjani and P. O'Brien, *Prog. Mater. Sci.*, 2017, **89**, 411–478.

20 Q. Ji, Y. Zheng, Y. Zhang and Z. Liu, *Chem. Soc. Rev.*, 2015, **44**, 2587–2602.

21 N. D. Boscher, C. J. Carmalt and I. P. Parkin, *Eur. J. Inorg. Chem.*, 2006, **2006**, 1255–1259.

22 S. L. Benjamin, Y. P. Chang, C. Gurnani, A. L. Hector, M. Huggon, W. Levason and G. Reid, *Dalton Trans.*, 2014, **43**, 16640–16648.

23 S. L. Benjamin, C. H. de Groot, C. Gurnani, S. L. Hawken, A. L. Hector, R. Huang, M. Jura, W. Levason, E. Reid, G. Reid, S. P. Richards and G. B. G. Stenning, *J. Mater. Chem. C*, 2018, **6**, 7734–7739.

24 P. J. McKarns, T. S. Lewkebandara, G. P. A. Yap, L. M. Liable-Sands, A. L. Rheingold and C. H. Winter, *Inorg. Chem.*, 1998, **37**, 418–424.

25 H. Wang, H. Yuan, S. Sae Hong, Y. Li and Y. Cui, *Chem. Soc. Rev.*, 2015, **44**, 2664–2680.

26 X. Duan, C. Wang, A. Pan, R. Yu and X. Duan, *Chem. Soc. Rev.*, 2015, **44**, 8859–8876.

27 X. Zhang, Z. Y. Al Balushi, F. Zhang, T. H. Choudhury, S. M. Eichfeld, N. Alem, T. N. Jackson, J. A. Robinson and J. M. Redwing, *J. Electron. Mater.*, 2016, **45**, 6273–6279.

28 Y. Sheng, H. Tan, X. Wang and J. H. Warner, *Chem. Mater.*, 2017, **29**, 4904–4911.

29 Y. Shi, H. Li and L. J. Li, *Chem. Soc. Rev.*, 2015, **44**, 2744–2756.

30 G. Malandrino, *Angew. Chem., Int. Ed.*, 2009, **48**, 7478–7479.

31 S. D. Reid, A. L. Hector, W. Levason, G. Reid, B. J. Waller and M. Webster, *Dalton Trans.*, 2007, **42**, 4769–4777.

32 N. D. Boscher, C. J. Carmalt and I. P. Parkin, *Chem. Vap. Deposition*, 2006, **12**, 54–58.

33 N. E. Richey, C. Haines, J. L. Tami and L. McElwee-White, *Chem. Commun.*, 2017, **53**, 7728–7731.

34 A. A. Tedstone, E. A. Lewis, N. Savjani, X. L. Zhong, S. J. Haigh, P. O'Brien and D. J. Lewis, *Chem. Mater.*, 2017, **29**, 3858–3862.

35 R. Huang, S. L. Benjamin, C. Gurnani, Y. Wang, A. L. Hector, W. Levason, G. Reid and C. H. De Groot, *Sci. Rep.*, 2016, **6**, 27593.

36 D. E. Smith, V. K. Greenacre, A. L. Hector, R. Huang, W. Levason, G. Reid, F. Robinson and S. Thomas, *Dalton Trans.*, 2020, **49**, 2496–2504.

37 Y. P. Chang, A. L. Hector, W. Levason and G. Reid, *Dalton Trans.*, 2017, **46**, 9824–9832.

38 C. Gurnani, S. L. Hawken, A. L. Hector, R. Huang, M. Jura, W. Levason, J. Perkins, G. Reid and G. B. G. Stenning, *Dalton Trans.*, 2018, **47**, 2628–2637.

39 Y. P. Chang, A. L. Hector, W. Levason, G. Reid and J. Whittam, *Dalton Trans.*, 2018, **47**, 2406–2414.

40 V. K. Greenacre, A. L. Hector, R. Huang, W. Levason, V. Sethi and G. Reid, *Dalton Trans.*, 2022, **51**, 2400–2412.

41 N. Kumari, M. Kalyan, S. K. Ghosh, A. R. Maity and R. Mukherjee, *Mater. Res. Express*, 2021, **8**, 45902.

42 J. H. Kim, S. Yu, S. W. S. Y. Lee, S. W. S. Y. Lee, K. S. Kim, Y. A. Kim and C. M. Yang, *Crystals*, 2020, **10**, 140.

43 P. Sumathi, J. Chandrasekaran, R. Marnadu, S. Muthukrishnan and S. Maruthamuthu, *J. Mater. Sci.: Mater. Electron.*, 2018, **29**, 16815–16823.

44 M. W. Iqbal, M. Z. Iqbal, M. F. Khan, M. A. Shehzad, Y. Seo, J. H. Park, C. Hwang and J. Eom, *Sci. Rep.*, 2015, **5**, 1–9.

45 A. Sebastian, R. Pendurthi, T. H. Choudhury, J. M. Redwing and S. Das, *Nat. Commun.*, 2021, **12**, 1–12.

46 K. Wu, C. Guo, H. Wang, X. Zhang, J. Wang and J. Chen, *Opt. Express*, 2017, **25**, 17639.

47 D. J. Gulliver, E. G. Hope, W. Levason, S. G. Murray, D. M. Potter and G. L. Marshall, *J. Chem. Soc., Perkin Trans. 2*, 1984, **3**, 429–434.

48 S. Graulis, D. Chateigner, R. T. Downs, A. F. T. Yokochi, M. Quirós, L. Lutterotti, E. Manakova, J. Butkus, P. Moeck and A. Le Bail, *J. Appl. Crystallogr.*, 2009, **42**, 726–729.

49 G. Bergerhoff, *Inorganic Crystal Structure Database (ICSD)*, FIZ Karlsruhe, **https://www.fiz-karlsruhe.de/en/produkte-und-dienstleistungen/inorganic-crystal-structure-database-icsd**, accessed 3 June 2021.

50 W. J. Schutte, J. L. De Boer and F. Jellinek, *J. Solid State Chem.*, 1987, **70**, 207–209.

51 D. Zhang, T. Liu, J. Cheng, Q. Cao, G. Zheng, S. Liang, H. Wang and M. S. Cao, *Nano-Micro Lett.*, 2019, **11**, 1–15.

52 C. Lan, C. Li, J. C. Ho and Y. Liu, *Adv. Electron. Mater.*, 2021, **7**, 2000688.

53 X. Zhang, X. F. Qiao, W. Shi, J. Bin Wu, D. S. Jiang and P. H. Tan, *Chem. Soc. Rev.*, 2015, **44**, 2757–2785.

54 X. Duan, C. Wang, Z. Fan, G. Hao, L. Kou, U. Halim, H. Li, X. Wu, Y. Wang, J. Jiang, A. Pan, Y. Huang, R. Yu and X. Duan, *Nano Lett.*, 2016, **16**, 264–269.

55 H. Zobeiri, S. Xu, Y. Yue, Q. Zhang, Y. Xie and X. Wang, *Nanoscale*, 2020, **12**, 6064–6078.

56 A. Berkdemir, H. R. Gutiérrez, A. R. Botello-Méndez, N. Perea-López, A. L. Elías, C. I. Chia, B. Wang, V. H. Crespi, F. López-Urías, J. C. Charlier, H. Terrones and M. Terrones, *Sci. Rep.*, 2013, **3**, 1–8.

57 Y. Fu, M. Long, A. Gao, Y. Wang, C. Pan, X. Liu, J. Zeng, K. Xu, L. Zhang, E. Liu, W. Hu, X. Wang and F. Miao, *Appl. Phys. Lett.*, 2017, **111**, 043502.

58 F. Bozheyev, K. Harbauer and K. Ellmer, *Sci. Rep.*, 2017, 7, 1–11.

59 Y. J. Noori, S. Thomas, S. Ramadan, V. K. Greenacre, N. M. Abdelazim, Y. Han, J. Zhang, R. Beanland,

9644 | *J. Mater. Chem. A*, 2023, **11**, 9635–9645

This journal is © The Royal Society of Chemistry 2023

A. L. Hector, N. Klein, G. Reid, P. N. Bartlett and C. H. De Groot, *2D Mater.*, 2022, **9**, 015025.

60 M. L. Zou, J. D. Chen, L. F. Xiao, H. Zhu, T. T. Yang, M. Zhang and M. L. Du, *J. Mater. Chem. A*, 2015, **3**, 18090–18097.

61 J. Guo, Y. Shi, X. Bai, X. Wang and T. Ma, *J. Mater. Chem. A*, 2015, **3**, 24397–24404.

62 R. Li, Y. Cheng and W. Huang, *Small*, 2018, **14**, 1802091.

63 M. S. Sokolikova, P. C. Sherrell, P. Palczynski, V. L. Bemmer and C. Mattevi, *Nat. Commun.*, 2019, **10**, 1–8.

64 Z. Huang, T. Wu, S. Kong, Q. L. Meng, W. Zhuang, P. Jiang and X. Bao, *J. Mater. Chem. A*, 2016, **4**, 10159–10165.

65 H. Kawai, M. Sugahara, R. Okada, Y. Maniwa, Y. Yomogida and K. Yanagi, *Appl. Phys. Express*, 2017, **10**, 15001.

66 W. Y. Kim, H. J. Kim, T. Hallam, N. McEvoy, R. Gatensby, H. C. Nerl, K. O'Neill, R. Siris, G. T. Kim and G. S. Duesberg, *Adv. Mater. Interfaces*, 2018, **5**, 1701161.

67 R. Kumar and N. Khare, *Thin Solid Films*, 2008, **516**, 1302–1307.

68 J. Yang, F. Bussolotti, H. Kawai and K. E. J. Goh, *Phys. Status Solidi RRL*, 2020, **14**, 2000248.

69 A. N. Enyashin, M. Bar-Sadan, L. Houben and G. Seifert, *J. Phys. Chem. C*, 2013, **117**, 10842–10848.

70 N. R. Pradhan, D. Rhodes, S. Memaran, J. M. Poumirol, D. Smirnov, S. Talapatra, S. Feng, N. Perea-Lopez, A. L. Elias, M. Terrones, P. M. Ajayan and L. Balicas, *Sci. Rep.*, 2015, **5**, 1–8.

71 L. Yang, K. Majumdar, H. Liu, Y. Du, H. Wu, M. Hatzistergos, P. Y. Hung, R. Tieckelmann, W. Tsai, C. Hobbs and P. D. Ye, *Nano Lett.*, 2014, **14**, 6275–6280.

72 F. Lan, R. Yang, K. Sun, Z. Wang, Y. Zhang, Y. Wang and H. Cheng, *Vacuum*, 2022, **201**, 111091.

73 D. Kim, H. Du, T. Kim, S. Shin, S. Kim, M. Song, C. Lee, J. Lee, H. Cheong, D. H. Seo and S. Seo, *AIP Adv.*, 2016, **6**, 105307.

74 H. Zhou, C. Wang, J. C. Shaw, R. Cheng, Y. Chen, X. Huang, Y. Liu, N. O. Weiss, Z. Lin, Y. Huang and X. Duan, *Nano Lett.*, 2015, **15**, 709–713.

75 G. Lee, S. Oh, J. Kim and J. Kim, *ACS Appl. Mater. Interfaces*, 2020, **12**, 23127–23133.

76 T. H. Tsai, Z. Y. Liang, Y. C. Lin, C. C. Wang, K. I. Lin, K. Suenaga and P. W. Chiu, *ACS Nano*, 2020, **14**, 4559–4566.

77 H. C. Kim, H. Kim, J. U. Lee, H. B. Lee, D. H. Choi, J. H. Lee, W. H. Lee, S. H. Jhang, B. H. Park, H. Cheong, S. W. Lee and H. J. Chung, *ACS Nano*, 2015, **9**, 6854–6860.

78 T. J. Seebeck, *Ann. Phys*, 1826, **82**, 253–286.

79 P. Scherrer, *Nachrichten von der Gesellschaft der Wissenschaften zu Göttingen, Mathematisch-Physikalische Klasse*, 1918, **1918**, 98–100.

80 Y. W. Gao, Y. Z. He and L. L. Zhu, *Chin. Sci. Bull.*, 2010, **55**, 16–21.

81 Y. Hu, T. Yang, D. Li, G. Ding, C. Dun, D. Wu and X. Wang, *ACS Omega*, 2021, **6**, 7879–7886.

This journal is © The Royal Society of Chemistry 2023

J. Mater. Chem. A, 2023, **11**, 9635–9645 | **9645**